

CURRENT SHEET ENERGETICS, FLARE EMISSIONS, AND ENERGY PARTITION IN A SIMULATED SOLAR ERUPTION

KATHARINE K. REEVES¹, JON A. LINKER², ZORAN MIKIĆ², AND TERRY G. FORBES³

¹ Harvard-Smithsonian Center for Astrophysics, 60 Garden Street, MS 58, Cambridge, MA 02138, USA; kreeves@cfa.harvard.edu

² Predictive Science, Inc. (PSI), 9990 Mesa Rim Road, Suite 170, San Diego, CA 92121-2910, USA; linkerj@predsci.com, mikicz@predsci.com

³ Institute for the Study of Earth, Oceans, and Space (EOS), University of New Hampshire, 8 College Road, Durham, NH 03824, USA; terry.forbes@unh.edu

Received 2010 April 13; accepted 2010 August 5; published 2010 September 10

ABSTRACT

We investigate coronal energy flow during a simulated coronal mass ejection (CME). We model the CME in the context of the global corona using a 2.5D numerical MHD code in spherical coordinates that includes coronal heating, thermal conduction, and radiative cooling in the energy equation. The simulation domain extends from 1 to $20 R_s$. To our knowledge, this is the first attempt to apply detailed energy diagnostics in a flare/CME simulation when these important terms are considered in the context of the MHD equations. We find that the energy conservation properties of the code are quite good, conserving energy to within 4% for the entire simulation (more than 6 days of real time). We examine the energy release in the current sheet as the eruption takes place, and find, as expected, that the Poynting flux is the dominant carrier of energy into the current sheet. However, there is a significant flow of energy out of the sides of the current sheet into the upstream region due to thermal conduction along field lines and viscous drag. This energy outflow is spatially partitioned into three separate components, namely, the energy flux flowing out the sides of the current sheet, the energy flowing out the lower tip of the current sheet, and the energy flowing out the upper tip of the current sheet. The energy flow through the lower tip of the current sheet is the energy available for heating of the flare loops. We examine the simulated flare emissions and energetics due to the modeled CME and find reasonable agreement with flare loop morphologies and energy partitioning in observed solar eruptions. The simulation also provides an explanation for coronal dimming during eruptions and predicts that the structures surrounding the current sheet are visible in X-ray observations.

Key words: magnetic reconnection – magnetohydrodynamics (MHD) – Sun: coronal mass ejections (CMEs) – Sun: flares

1. INTRODUCTION

One of the most intriguing questions in solar physics is how energy is released during a coronal mass ejection (CME). A typical CME releases on the order of 10^{32} erg of energy (e.g., Forbes 2000), and this energy is partitioned into the kinetic energy of the plasma released into the heliosphere, work done against gravity as the CME is ejected, heating of the associated flaring loops, and radiation loss. Estimates from observations (Forbes 2000; Emslie et al. 2005) suggest that similar amounts of energy go into heating the flare plasma and accelerating the CME, but the uncertainties in these estimates are large.

Many authors have used numerical models of CMEs to address the question of the energy release by calculating global energetics in simulated eruptions (e.g., Mikić & Linker 1994; Linker et al. 2003; Manchester et al. 2004; MacNeice et al. 2004; Fan & Gibson 2007; Chen et al. 2007). These calculations are useful for, e.g., determining the relationship between the open and stored magnetic energy (Linker et al. 2003) required for an eruption, or the difference in magnetic energy release between eruptions initiated with the torus and kink instabilities (Fan & Gibson 2007). However, until now, no attempt has been made to track the conversion of magnetic energy into thermal energy, including the effects of conduction and radiation, as the magnetic field undergoes reconnection in the current sheet. Quantifying the amount of thermal energy released in an eruptive event and addressing the effects of conduction and radiation are crucial steps for understanding observations of flare emissions.

A previous quasi-analytical model of CME initiation addressed the energy conversion in the current sheet in eruptive

events by assuming that the Poynting flux into the current sheet is completely thermalized (Reeves & Forbes 2005; Reeves et al. 2007). This model produces realistic flare emissions, but many simplifying assumptions are employed, including the assumption that the Poynting flux is completely transformed into thermal energy, and that the thermal energy flux is equally distributed such that half is directed toward the CME and half is directed toward the flare loops. Recent analytical calculations by Seaton (2008) of an asymmetrical current sheet suggest that, in fact, this energy is not equally partitioned, but that more energy is directed toward the CME. The configuration used by Seaton (2008) consists of a flux rope on one end and reconnected flare loops on the other, and in this case, he finds that the X-point is not located at the center of the current sheet, but rather stays close to the Sun's surface during the entire eruption, causing the energy partition to be unequal.

Energy conversion in CMEs has also been addressed using numerical simulations that employ simplified energy equations (Birn et al. 2008, 2009). These studies find that the dominant energy transfer consists of a conversion of the incoming Poynting flux to enthalpy flux in the sunward direction and bulk kinetic energy in the CME direction. These simulations, however, neglect radiation, conduction, and coronal heating in the energy equation, terms which are certainly important in the energy transfer in flare loops and solar eruptions.

In this paper, we simulate a CME using a 2.5D MHD numerical model that incorporates features not present in the analytic model of Reeves & Forbes (2005). The simulation is performed in the context of the global corona, in a spherical coordinate domain that extends from 1 to $20 R_s$. We first solve the MHD equations to develop an equilibrium helmet

streamer configuration (Linker & Mikić 1995). This model also employs a realistic energy equation that includes conduction, radiative losses, and coronal heating. Thus, we are able to self-consistently follow the energy flow in the corona during a CME. To our knowledge, a calculation of the energy budget this detailed has not been done before. Details of the model are given in Section 2. Section 3 explains the details of the energy calculation, and the results and discussion are given in Section 4. Conclusions are presented in Section 5.

2. MODEL DESCRIPTION

The MHD coronal code MAS includes a realistic energy equation that includes the effects of thermal conduction, radiation, and coronal heating (Mikić et al. 1999). The model solves the following form of the MHD equations in spherical coordinates:

$$\nabla \times \mathbf{B} = \frac{4\pi}{c} \mathbf{J}, \quad (1)$$

$$\frac{1}{c} \frac{\partial \mathbf{B}}{\partial t} = -\nabla \times \mathbf{E}, \quad (2)$$

$$\mathbf{E} + \frac{1}{c} \mathbf{v} \times \mathbf{B} = \eta \mathbf{J}, \quad (3)$$

$$\frac{\partial \rho}{\partial t} + \nabla \cdot (\rho \mathbf{v}) = 0, \quad (4)$$

$$\rho \left(\frac{\partial \mathbf{v}}{\partial t} + \mathbf{v} \cdot \nabla \mathbf{v} \right) = \frac{1}{c} \mathbf{J} \times \mathbf{B} - \nabla p + \rho \mathbf{g} + \nabla \cdot (\nu \rho \nabla \mathbf{v}), \quad (5)$$

$$\frac{1}{\gamma - 1} \left(\frac{\partial P}{\partial t} + \nabla \cdot P \mathbf{v} \right) = -P \nabla \cdot \mathbf{v} + S, \quad (6)$$

where S consists of the heat sources and sinks:

$$S = -\nabla \cdot \mathbf{q} - n_e n_p Q(T) + H_{ch} + H_\eta. \quad (7)$$

In the above equations, \mathbf{B} is the magnetic field, \mathbf{J} is the electric current density, \mathbf{E} is the electric field, ρ , \mathbf{v} , p , and T are the plasma mass density, velocity, pressure, and temperature, respectively, $\mathbf{g} = -g_0 \hat{\mathbf{r}} R_s^2 / r^2$ is the gravitational acceleration (with R_s the solar radius), η is the resistivity, ν is the kinematic viscosity, and k is Boltzmann's constant. The method of solution of Equations (1)–(7) has been discussed in detail in previous papers, including simulations that incorporate the transition region and upper chromosphere in the domain of the calculation, as is the case here (Mikić & Linker 1994; Linker & Mikić 1997; Lionello et al. 1999, 2001; Mikić et al. 1999; Linker et al. 2001, 2003).

In the equations governing energy conservation, Equations (6) and (7), $Q(T)$ is a standard radiative loss function that has a maximum near 10^5 K (see Athay 1986), n_e and n_p are the electron and proton number density (which are assumed to be equal for the case of a hydrogen plasma treated here), m is the proton mass, $\gamma = 5/3$ is the ratio of specific heats, and $H_\eta = \eta J^2$ is the ohmic heating term. Since it is presently not known in detail what heats the corona, the coronal heating term H_{ch} is a parameterized function. The form used in these simulations is given by

$$H_{ch} = H_0 e^{-r/\lambda} + \frac{c_1}{2} \left[1 + \tanh \left(\frac{B/B_0 - c_2}{c_3} \right) \right] \left(\frac{B}{B_0} \right)^{c_4}, \quad (8)$$

where H_0 , λ , c_1 , c_2 , c_3 , and c_4 are parameters. In this case, $H_0 = 1.07 \times 10^{-6}$ erg cm $^{-3}$ s $^{-1}$, $B_0 = 2.2$ G, $\lambda = 0.7 R_s$, $c_1 = 1.34 \times 10^{-5}$ erg cm $^{-3}$ s $^{-1}$, $c_2 = 1.3$, $c_3 = 0.25$, and $c_4 = 1$. The first term in Equation (8) is similar to coronal heating formulations used previously (Lionello et al. 2001; Linker et al. 2001), and the second term simulates active region heating in strong field regions.

The thermal conduction term in the energy equation is collisional (i.e., Spitzer) in the lower corona, and collisionless (see Hollweg 1978) higher up (Lionello et al. 2001), using the following equations:

$$\mathbf{q} = \begin{cases} -\kappa_0 T^{5/2} \hat{\mathbf{b}} \cdot \nabla T & r \lesssim 10 R_{\text{sun}} \\ \frac{1}{(\gamma-1)} n_e k T \mathbf{v} & r \gtrsim 10 R_{\text{sun}} \end{cases}, \quad (9)$$

where $\kappa_0 = 9 \times 10^{-7}$ erg K $^{-7/2}$ cm $^{-1}$ s $^{-1}$ and $\hat{\mathbf{b}}$ is the unit vector along \mathbf{B} . The function varies between the two forms of the conduction smoothly, with the contribution from the collisional conductivity varying as $0.5(1 - \tanh[0.2r - 2])$ and the contribution from the collisionless conductivity varying as $0.5(1 + \tanh[0.2r - 2])$, where r is in solar radii.

A typical reference value for the Alfvén speed at the base of the model corona is $V_A = 480$ km s $^{-1}$ (corresponding to $|B| = 2.2$ G and $n_0 = 10^8$ cm $^{-3}$). Therefore, the Alfvén travel time (τ_A) is 1446 s for a distance of $1 R_s$. The resistivity, η , is uniform throughout the simulation region and corresponds to a resistive diffusion time $\tau_R = 8 \times 10^4$ hr (for a length scale of $1 R_s$). Thus, the Lundquist number, which is given by $S_L = \tau_R / \tau_A = 4\pi R_s^2 / \tau_A \eta c^2$, has a value of 2×10^5 . This number is much smaller than the canonical value for the solar corona, which is typically taken to be on the order of 10^8 or larger (Craig & Litvinenko 2009), and thus the resistivity is much larger in the simulations than in the real corona. However, the value of η does not seem to affect the overall evolution of the magnetic field (Mikić & Linker 1994; Linker et al. 1999). An extensive discussion of the effect of this large resistivity on the MHD equations can be found in Mikić & Linker (1994). The kinematic viscosity, ν , is also uniform, and it has a value of 3.4×10^{15} cm 2 s $^{-1}$. This value corresponds to a viscous diffusion time, $\tau_\nu = R_s^2 / \nu$, of approximately $10^3 \tau_A$.

The primary complication that arises from realistic modeling of the heating terms in Equation (7) is that the balance between the thermal conduction of heat from the corona and radiative losses lower in the atmosphere produces a transition region in which the temperature and density gradients are extremely steep. These gradients lead to unrealistically long computing times in a region in which the details of the steep gradients are not as important as the fact that they are steep. We reconcile this problem by using a technique that artificially broadens the transition region, but maintains accurate values in the corona. The analysis done by Lionello et al. (2009) shows that to broaden the transition region, κ needs to be increased and $Q(T)$ decreased at low temperatures such that the product $\kappa(T)Q(T)$ is unchanged. It is important to emphasize here that Lionello et al. (2009) find for one-dimensional calculations, this modification has the effect of broadening the transition region so that gradients there are computationally manageable, while at the same time, the solution in the corona does not change significantly from cases where this modification is not used. In our simulation, for temperatures below $T_c = 500,000$ K, we modify $\kappa(T)$ by multiplying by a factor of $(T_c/T)^3$ and we divide $Q(T)$ by that same factor in order to keep $\kappa(T)Q(T)$ constant.

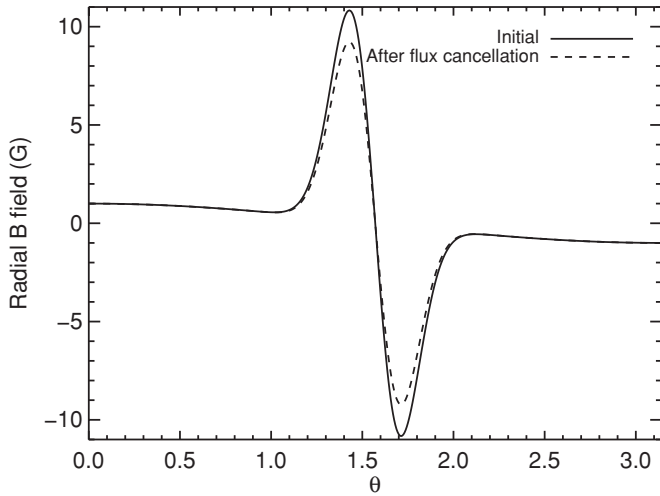


Figure 1. B_r as a function of θ at the lower boundary ($r = R_s$) initially (solid line), and after the flux cancellation is finished (dashed line).

The initial and boundary conditions for the code are as follows. The radial component of the magnetic field is specified at the lower boundary, where $r = R_s$. In these simulations, we use the sum of a weak dipole field and a stronger bipole ($B_{r, \text{obip}} = 10$ G) that is centered on the Sun's equator as the initial magnetic field state. We plot the initial radial magnetic field at R_s as a function of θ in Figure 1. The treatment of the plasma density and temperature in a calculation incorporating the transition region, including the initial and boundary conditions, is described in detail by Lionello et al. (2009). For this calculation, a temperature of 50,000 K and a number density of $5 \times 10^{12} \text{ cm}^{-3}$ were specified. These numbers in fact constitute an overestimate of the pressure in the lower transition region. As discussed by Lionello et al. (2009), the exact value does not determine the temperature and density in the coronal portion of the solution (the specified coronal heating does), and an overestimate is best to prevent evaporation of the chromosphere if strong heating is present. The component of the velocity parallel to the magnetic field is not specified but calculated using the characteristic equations. A spherically symmetric solar wind solution for the specified heating is used as the initial condition for the plasma. At the upper radial boundary, at $20 R_s$, the flow is supersonic and super-Alfvénic, and the characteristic equations are used for the boundary conditions such that only outgoing waves are allowed there. The characteristic boundary conditions allow plasma and magnetic fields to flow freely out of the simulation domain. More details on the implementation of the boundary conditions can be found in Linker & Mikić (1997), Mikić et al. (1999), and Linker et al. (2001).

Equations (1)–(9) are solved on a nonuniform mesh that allows us to concentrate grid points in regions of interest. For this work, we use a grid with a spatial resolution of 400×500 points on an $r - \theta$ mesh designed to have highest spatial resolution at the equator, where the current sheet forms. In this case, $\Delta\theta = 0.00117$ radians at the equator and it increases linearly with θ to $\Delta\theta = 0.045$ between $\theta = 1.41$ and $\theta = 0$ radians and between $\theta = 1.72$ and $\theta = \pi$ radians. The value of Δr is $0.00052 R_s$ at the solar surface and it varies linearly with r . At the outer boundary, $r = 20 R_s$, $\Delta r = 0.3 R_s$.

There are several phases of evolution in this simulation that culminate in the eruption of a flux rope. First, we impose a spherically symmetric solar wind solution on the initial magnetic

field configuration and integrate the time-dependent MHD equations until an equilibrium is reached at $200 \tau_A$. This process forms a helmet streamer, as in Linker & Mikić (1995), Linker et al. (2001), and Linker et al. (2003). Then, a shear flow is introduced in the ϕ direction as follows: v_ϕ is linearly increased from zero to 1.9 km s^{-1} from 200 to $210 \tau_A$, held constant at 1.9 km s^{-1} until $275 \tau_A$, and then decreased linearly back to zero from 275 to $285 \tau_A$. This shear flow introduces a shear in the magnetic fields in the ϕ direction, allowing magnetic energy to build in the system. Finally, flux cancellation is initiated at the boundary by linearly decreasing the strength of the bipole term in the initial magnetic field configuration from 10 G to 8.5 G between 285 and $305 \tau_A$. The final state of the radial magnetic field at the lower boundary after the flux cancellation finishes is shown as a dashed line in Figure 1. This cancellation causes a flux rope to form, lose equilibrium, and erupt. The process used here is similar to the simulated eruption using the polytropic version of the same code reported by Linker et al. (2003).

3. ENERGY INTEGRAL FOR THE SIMULATION DOMAIN

We investigate energy flow in the simulation, including energy flow into and out of the domain and into and out of specific regions of interest. In order to do so, we rewrite Equation (6) in the following way:

$$\frac{\partial}{\partial t} \left(\frac{P}{\gamma-1} + \frac{\rho v^2}{2} + \frac{B^2}{8\pi} \right) + \nabla \cdot \left[\left(\frac{\gamma P}{\gamma-1} + \frac{\rho v^2}{2} \right) \mathbf{v} + \frac{c}{4\pi} \mathbf{E} \times \mathbf{B} \right] = -\nabla \cdot \mathbf{q} - n_e n_p Q(T) + H_{ch} + \mathbf{v} \cdot \mathbf{F}, \quad (10)$$

where \mathbf{F} represents the forces due to viscosity and gravity, and we have used the fact that

$$\frac{1}{c} \mathbf{v} \cdot \mathbf{J} \times \mathbf{B} + \eta J^2 = -\frac{c}{4\pi} \nabla \cdot (\mathbf{E} \times \mathbf{B}) - \frac{\partial}{\partial t} \left(\frac{B^2}{8\pi} \right). \quad (11)$$

We integrate both sides of Equation (10) over the specified volume and apply the divergence theorem to get the following equation:

$$\begin{aligned} & \int \frac{\partial}{\partial t} (\mathcal{E} + \mathcal{K} + \mathcal{W}) dV \\ & = - \int (n_e n_p Q(T) - H_{ch} - \rho \mathbf{v} \cdot \mathbf{g} + \nu \rho \nabla \mathbf{v} : \nabla \mathbf{v}) dV \\ & - \int \left[\left(\frac{\gamma P}{\gamma-1} + \frac{\rho v^2}{2} \right) \mathbf{v} + \frac{c}{4\pi} \mathbf{E} \times \mathbf{B} + \mathbf{q} - \nu \rho \nabla \mathbf{v} \cdot \mathbf{v} \right] \cdot d\mathbf{A}, \end{aligned} \quad (12)$$

where the colon indicates a double-dot product. In this case, \mathcal{E} , \mathcal{K} , and \mathcal{W} are the internal, kinetic, and magnetic energy densities, respectively, ν is the kinematic viscosity, and we have used the relationship

$$\mathbf{v} \cdot \mathbf{F}_v = \mathbf{v} \cdot \nabla \cdot (\rho \nu \nabla \mathbf{v}) = \nabla \cdot (\nu \rho \nabla \mathbf{v} \cdot \mathbf{v}) - \nu \rho \nabla \mathbf{v} : \nabla \mathbf{v}, \quad (13)$$

where \mathbf{F}_v is the viscous force. Note that all of the terms that involved volume integrals of divergences in Equation (12) have been converted into surface integrals using the divergence theorem, and these integrals are used to calculate energy flow over the surface of the simulation domain. We are able to calculate all the terms in Equation (12) directly from outputs of the simulations, and we describe the results of those calculations over the entire simulation domain as well as in the local area of the current sheet in the next section.

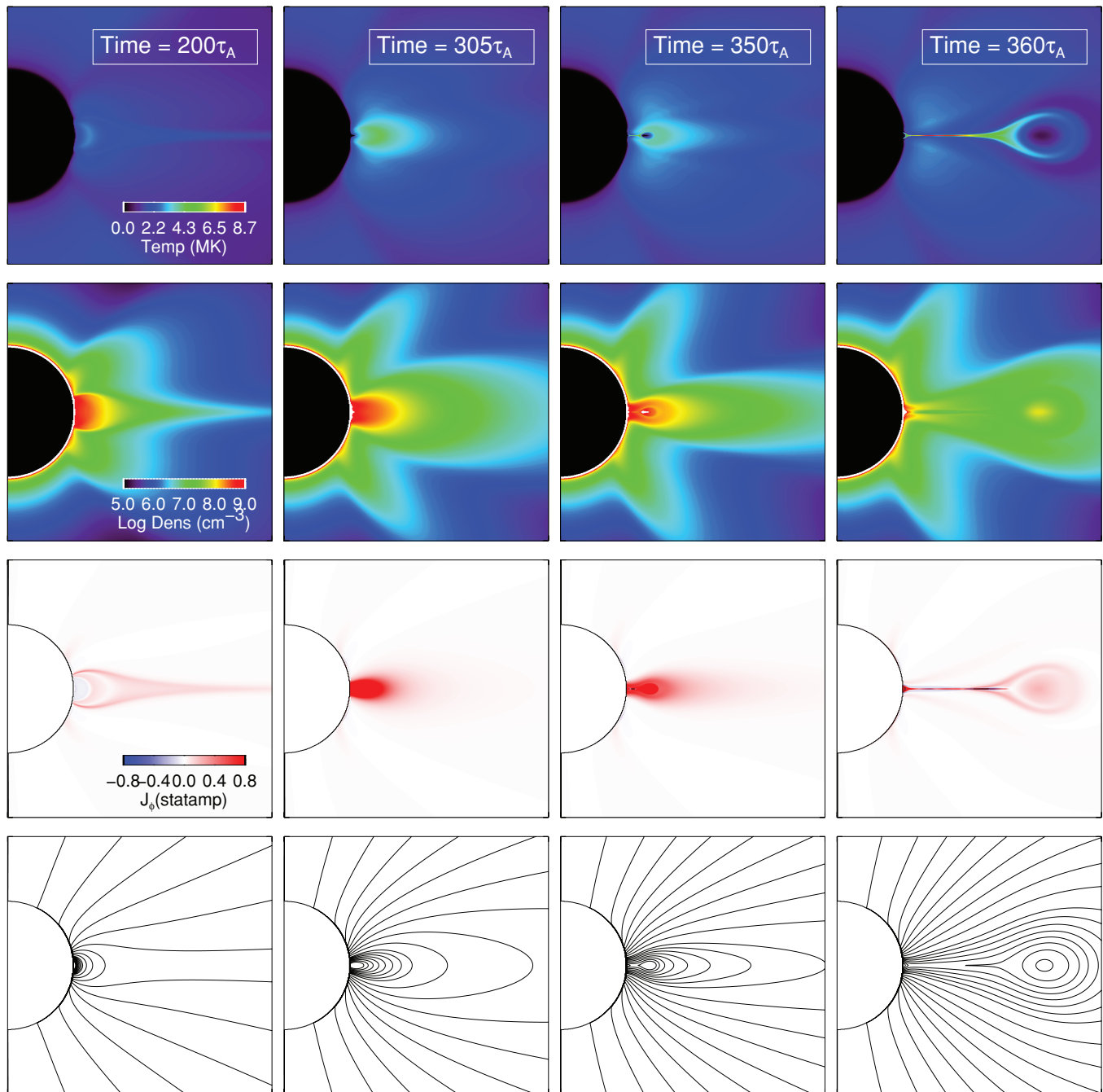


Figure 2. Temperature (top panels), density (second row), toroidal current (third row), and flux contours (bottom panels) for several times during the simulation. The times chosen are at the end of the relaxation phase ($200 \tau_A$), at the end of the flux cancellation phase ($305 \tau_A$), just after the formation of the current sheet ($350 \tau_A$) and later in the eruptive phase ($360 \tau_A$). A magnetic field component perpendicular to the plane of the figure (B_ϕ) is also present. The entire simulation domain spans from 1 to $20 R_{\text{sun}}$. Each frame in this figure shows a portion of that domain, extending to $5 R_s$ on the right-hand side and -2.5 to $2.5 R_s$ on the top and bottom.

4. RESULTS AND DISCUSSION

A summary of the evolution of the temperature, the current density in the ϕ direction, and the density during the simulation is shown in Figure 2. The first column on the left in Figure 2 shows these quantities in the helmet streamer at the end of the equilibration phase, which lasts from 0 to $200 \tau_A$. The second column shows the parameters at the end of the flux cancellation phase, which is initiated at $285 \tau_A$ and continues until $305 \tau_A$. During this period, 15% of the flux is canceled, and a flux rope is formed that contains field line dips that are capable of supporting plasma from the chromosphere. Because we are

employing a realistic energy equation in our calculations, the flux rope contains cool and dense prominence-like material.

The two rightmost columns in Figure 2 show the formation of an X-point below the flux rope and the subsequent eruption after equilibrium is lost. Associated with the eruption is a long current sheet. Evidence for such long current sheets has been found in observations from the Large Angle and Spectrometric Coronagraph (Ko et al. 2003; Lin et al. 2005) on *Solar and Heliospheric Observatory (SoHO)* and the *Reuven Ramaty High Energy Solar Spectroscopic Imager* (Sui & Holman 2003). Because of the large value of η used in the simulations, the current sheet may be broader than those formed in the corona.

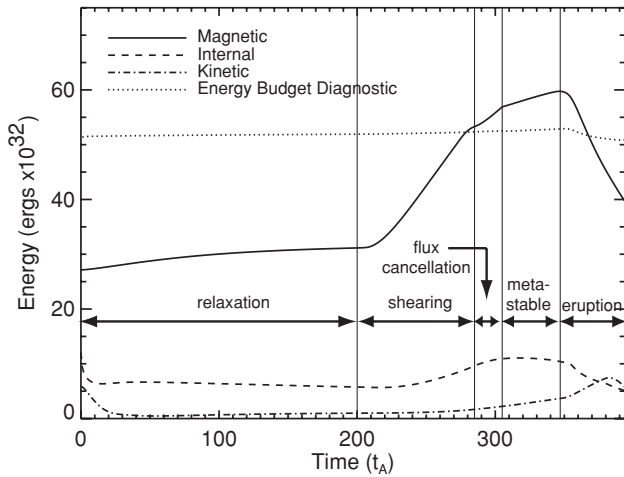


Figure 3. Magnetic energy (solid line), internal energy (dashed line), kinetic energy (dash-dotted line) over the entire simulation volume. Also included is the energy budget diagnostic (dotted line), which is derived from integrating all of the terms in Equation (12) as a function of time. The nearly constant value of this quantity indicates that energy is conserved.

However, a recent study has suggested that CME-trailing current sheets in the corona may be broader than expected due to turbulence and the presence of the tearing mode instability (Lin et al. 2007).

4.1. Energy Flow for the Full Simulation Volume

In Figure 3, we plot the magnetic, kinetic, and internal energy (\mathcal{W} , \mathcal{K} , and \mathcal{E} in Equation (12), integrated over the simulation volume) as a function of time over the entire simulation volume. The magnetic energy shows a slow increase during the streamer relaxation phase due to opening of previously closed potential field lines by the solar wind. As in previous simulations of erupting flux ropes (Linker et al. 2001, 2003), we shear the magnetic field (from 210 to 285 τ_A) in order to build up magnetic energy in the streamer. Figure 3 shows that during the shearing phase, the magnetic energy increases from about 30×10^{32} erg to about 50×10^{32} erg.

The magnetic energy continues to increase slowly after the flux cancellation is stopped. In this simulation, we have stopped the flux cancellation very close to the marginal stability point of the flux rope. Continued flux cancellation would lead to the eruption of the flux rope, but in the simulation reported here, we let the flux rope destabilize due to the small resistive diffusion. The finite resistivity in the simulation causes the current to decrease in the flux rope, which leads to a slow rise in the flux rope between $t = 305 \tau_A$ and $t = 347 \tau_A$, and its eventual destabilization and eruption at $347 \tau_A$. We refer to this phase as the metastable phase.

After the eruption at $347 \tau_A$, a current sheet forms underneath the ejected flux rope. During this final phase of the simulation, the magnetic energy decreases from about 60×10^{32} erg to about 40×10^{32} erg. The kinetic energy increases by about 4×10^{32} erg during this phase as the CME accelerates. The rest of the magnetic energy released goes into the gravitational potential energy of the flux rope, and heating the plasma in the corona.

In order to check the accuracy of the numerical method, we assess the overall energy conservation in our algorithm. The quantity labeled “Energy Budget Diagnostic” in Figure 3 is found at each time step by integrating all of the terms in Equation (12) as a function of time to get energy, and then

summing them. This diagnostic includes the magnetic, internal, and kinetic energy plotted in Figure 3, as well as viscous dissipation, work done against gravity, changes in energy due to radiation and heat sources, and the energy deposited in or carried away from the simulation domain due to flows, e.g., conductive flux, kinetic energy flux, enthalpy flux, and Poynting flux. Thus, we have accounted for all the changes in energy in the simulation volume, as well as the energy that enters and exits the simulation volume over the boundary. In a perfect code, this sum would be a constant as a function of time, indicating that energy is conserved.

We find that during the relaxation, shearing, flux cancellation, and metastable phases, energy is conserved quite well by the code. During these phases, the total energy calculated by our diagnostics is within 3% of the initial energy. This result is quite good, considering that the total run time T is more than 300 Alfvén scale times and that there is significant energy transfer in the system during these phases of the simulation.

The eruptive phase of the simulation is the phase in which most of the energy losses occur. During this phase, the total calculated energy is decreased by about 4% of the pre-eruption energy. These losses are primarily due to the additional numerical resistivity introduced by the use of upwind derivatives of advective terms, which has the effect of diffusing the steep gradients that appear when the current sheet is present. If these losses were considered to be entirely due to numerical resistivity, the effective Lundquist number during the eruptive phase would be approximately $S_L = 1.6 \times 10^5$, rather than the imposed value of $S_L = 2 \times 10^5$.

For the energy diagnostics shown in Figure 3, we calculate the energy over the entire simulation domain. We have also calculated the energy over several sub-domains, where different parts of the energy equation dominate. We find that the majority of the error in the diagnostics during the non-eruptive phases of the evolution is present in a sub-domain that contains the transition region, with boundaries $r_0 = 1 R_s$ and $r_1 = 1.03 R_s$. In this region, radiation and conduction dominate the other energy terms, and small discretization errors in the calculation of these terms dominate the errors. In the sub-domain containing the corona and the heliosphere ($r_0 = 1.03 R_s$ to $r_1 = 20 R_s$), radiation and conduction no longer constitute the biggest contribution to the energy, and the total energy calculated by our diagnostics is within 1% of the initial energy in this sub-domain, except during the eruption.

The good energy conservation properties of the code allow us to make meaningful interpretations of energy flow and conversion in the simulation. In particular, the major conversion of magnetic energy (20×10^{32} erg) into kinetic, thermal, and other forms is significantly larger than the energy error ($\sim 2 \times 10^{32}$ erg).

Figure 4 shows the coronal heating, radiation, and conduction terms from the energy equation for the whole simulation volume. During the streamer formation phase, these terms remain relatively constant. The coronal heating term (which is proportional to $|B|$) begins to rise during the shear phase, due to the introduction of the longitudinal component of the magnetic field, B_ϕ . During the flux cancellation phase, it continues to rise, but not as steeply. Just after the formation of the current sheet, there is a spike in the coronal heating term as the eruption transports magnetic field farther out into the corona. Then, the heating decreases as the eruption proceeds and the magnetic fields surrounding the flux rope become weaker.

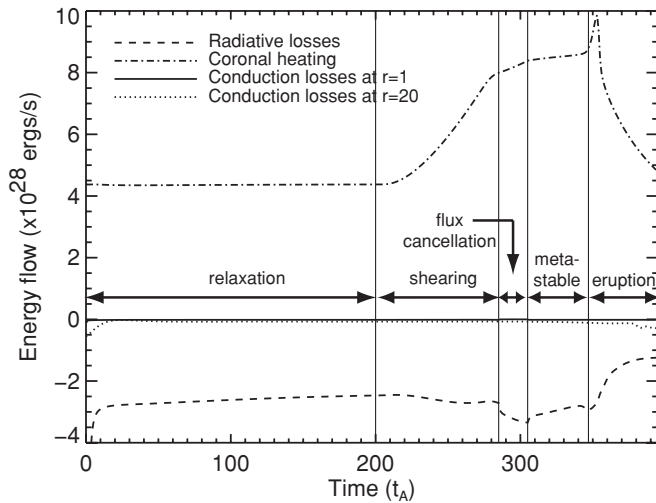


Figure 4. Conduction losses at $r = R_s$ (solid line) and $r = 20 R_s$ (dotted line), coronal heating (dash-dotted line), and radiative loss (dotted line) terms integrated over the entire simulation volume.

The largest radiative losses occur during the flux cancellation phase, when dense material at several hundred thousand degrees K is injected into the corona during the formation of the prominence-like region. After the eruption of this region and the formation of the current sheet, the radiative losses decrease as the plasma in the flare arcade heats up and the prominence-like material disperses. The conductive losses are surface terms in Equation (12), and so we show these losses at the boundaries of the simulation volume at $r = R_s$ and $r = 20 R_s$. There are no significant losses due to conduction at these boundaries.

4.2. Energy Flow in the Current Sheet

In order to ascertain the details of the energy conversion occurring in the current sheet during the evolution of the eruption, we draw a control volume around the current sheet and calculate the energy flow over its boundaries, using the surface integral term in Equation (12). The energy flow over the

boundaries of the control volume includes energy flow due to conductive heat flux, Poynting flux, enthalpy flux, kinetic energy flux, and viscous energy flux. The coronal heating, radiation, gravitational potential energy, and the change in the internal, kinetic and magnetic energies contribute to the rate of change of the energy in the volume of the current sheet.

We first calculate the energy estimate in a fixed control volume centered on the equator in the region of the current sheet to ensure that energy is conserved. The r boundaries of this control volume are set at $r_0 = 1.03 R_s$ and $r_1 = 2.0 R_s$. The control volume has a width of 12 mesh points in the θ direction, and it has an annulus shape because the numerical code is symmetric in the ϕ direction. The r and θ boundaries of the control volume are shown schematically in Figure 5. In this small, fixed control volume, we find that the energy is constant during the times preceding the eruption. During the formation of the current sheet, the losses are well accounted for by increased numerical dissipation, as in the larger volume described in the last section.

We next examine the energy flows in the current sheet as a function of time. Because we need to follow the evolution of the current sheet, we must define a control volume that changes with time. This changing control volume makes the energy conservation harder to follow, but the calculations with the static control volume give us confidence that energy is being conserved. The current sheet is growing as a function of time in our simulations, so the length of the control volume surrounding the sheet changes with time. We define the r boundaries of the control volume as the r values where there are minima in J_ϕ on either side of the maximum value. The values of r_0 and r_1 are initially $1.036 R_s$ and $1.1 R_s$, respectively, at $\tau_A = 347$. Like the static control volume described above, the current sheet control volume has a width in the θ direction of 12 mesh points and is annular in shape. We calculate the energy flux over the boundaries of the control volume in the rest frame of the Sun, since we are ultimately interested in the energy flux available to the post-flare loops for heating.

The calculated energy flow in and out of the control volume for our simulations is shown in Figure 6. There is a net inflow of energy into the current sheet in the θ direction, and there is a

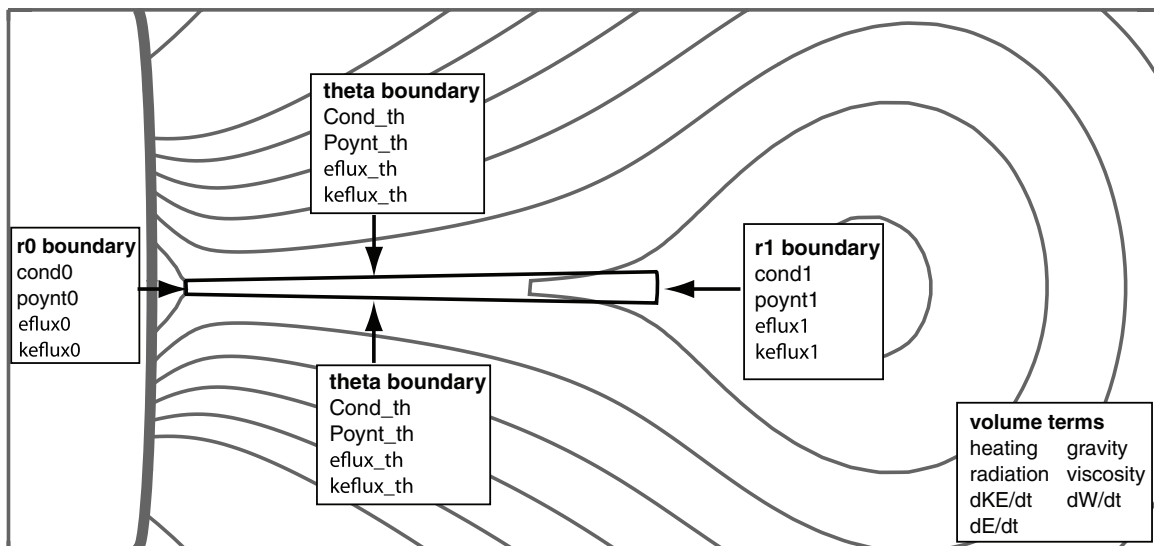


Figure 5. Flux contours from a portion of the simulation overlaid with the location of the control volume containing the current sheet. We label the boundary closest to the Sun's surface as r_0 and the boundary farthest from the surface as r_1 . For the fixed control volume, $r_0 = 1.03 R_s$ and $r_1 = 2.0 R_s$. For the current sheet control volume, r_0 and r_1 are initially at $1.036 R_s$ and $1.1 R_s$, respectively, and they change as the current sheet evolves.

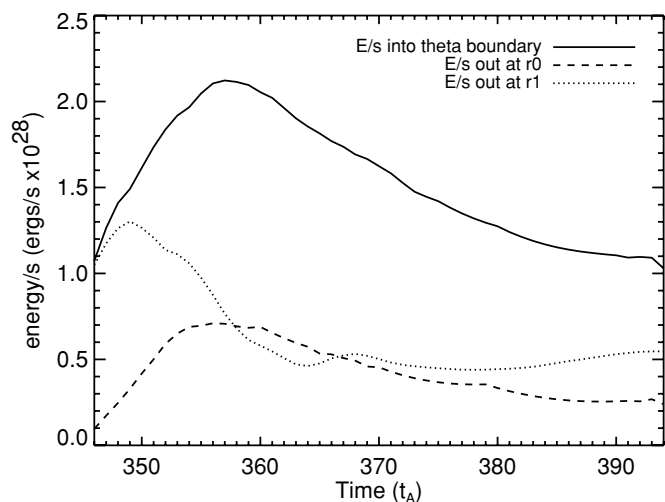


Figure 6. Total energy flow over the θ (solid line), $r0$ (dashed line), and $r1$ (dotted line) boundaries. There is a net flow of energy into the θ boundary and out of the r boundaries.

net outflow of energy at the $r0$ and $r1$ boundaries. Immediately after onset almost all of the outflow energy is channeled through the upper boundary at $r1$. During the intermediate stages of the evolution, the amounts of energy exiting the current sheet over the two r boundaries are similar, and in the later stages the energy flow at $r1$ exceeds the energy flow at $r0$ by about a factor of 2.

In Figure 7, we show the total energy flow over the two θ boundaries of the control volume encompassing the current sheet. The major contribution to the inflow of energy over this boundary is the Poynting flux, which is carried into the current sheet with the reconnecting magnetic fields. Kinetic energy due to reconnection inflow contributes to the influx of energy over the θ boundary as well, but this energy flow is small compared to the Poynting flux because the velocity in the upstream region is small.

Near the peak of the energy release, approximately half of the incoming Poynting flux is converted into heat conduction and viscous flow. The heating of the plasma in the current sheet generates a significant heat flux through the theta boundary of the current sheet because of the field-aligned thermal conduction. This heat flux is responsible for the relatively large width of the high-temperature structure below the flux rope visible in Figure 2 and is consistent with previous calculations that show that conduction is responsible for a thermal halo that extends outside the boundaries of the current sheet (Yokoyama & Shibata 1997; Seaton & Forbes 2009). There is also a significant transport of energy from the current sheet into the upstream region because of viscous drag. The high-speed outflow within the current sheet drags some of the outside plasma along with it. The kinetic energy added to the upstream flow by this means is labeled as “viscosity” in Figure 7. The shear viscosity in the code that causes this effect is very likely much larger than that which occurs in the corona actually (see Hollweg 1986). The shear viscosity, like the electrical resistivity, is so small in the corona that it cannot be realistically modeled in present-day simulations.

Previous work used a semi-analytical loss-of-equilibrium CME model to determine the energy input into post-flare loops (Reeves & Forbes 2005; Reeves et al. 2007). While conductive losses are considered in the evolution of the flare loops in these models, the conduction of heat out of the current sheet is not explicitly calculated. Instead, it is simply assumed that half of

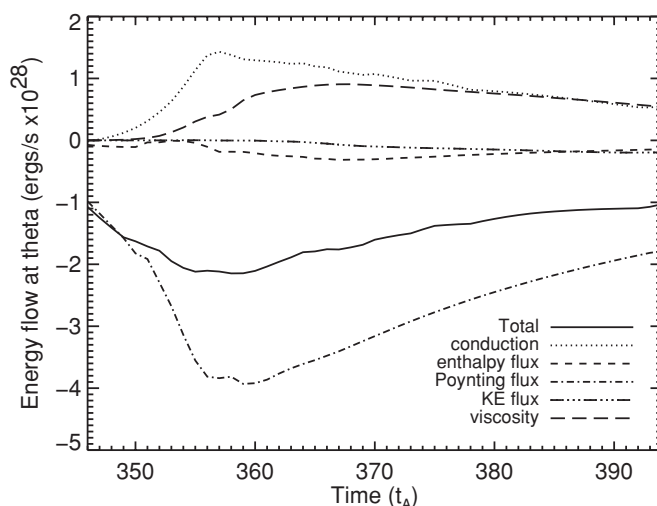


Figure 7. Energy flow over the θ boundary. Shown are the total energy (solid line), the conduction flux (dotted line), the enthalpy flux (short-dashed line), the Poynting flux (dot-dashed line), the kinetic energy flux (dot-dot-dashed line), and the viscosity (long-dashed line). Negative values indicate energy flow into the sheet, and positive values indicate energy flow out of the sheet.

the Poynting flux into the current sheet is somehow deposited into the flare loops. Figure 7 shows that the fraction of the heat flux through the sides of the current sheet varies considerably with time. Furthermore, not all of this energy necessarily reaches the surface. In our 2.5D simulation, most of the field lines threading the current sheet lie above the X-line, and these lines are contained within a magnetic island that does not reach the surface.

In Figure 8, we show the different types of energy that flow across the boundaries at $r0$ and $r1$. For the lower boundary, $r0$, the majority of the energy flowing over the sunward boundary of the control volume is conductive heat flux. There is also a small amount of the Poynting flux through the lower boundary early in the event. The kinetic energy flux is not shown for the $r0$ boundary in Figure 8(a) because it is several orders of magnitude smaller than the other terms.

The conductive energy flux through the $r0$ boundary is the energy flux available for heating of the plasma in the flare loops. Integrating this energy flux over the duration of the eruption gives an energy of approximately 3.0×10^{32} erg. It must be remembered, however, that this simulation is axisymmetric, and thus models a flux rope ringing the Sun. In order to compare the energy release to real events, we take a portion of the flare arcade with a typical length of 100,000 km. For this flare arcade, our model gives a total conductive energy flux through the $r0$ boundary of 6.8×10^{30} erg. Estimates from observations typically give a value for the thermal energy in the flare loops on the order of 1×10^{31} erg (Moore et al. 1980; Emslie et al. 2005), although these numbers can vary by as much as an order of magnitude or two based on factors such as the magnetic field strength. Given this variation in observed thermal energies in flares, the simulation produces a reasonable amount of energy to produce the heating observed in flare loops. More discussion about the energy partition is given in the next section.

We show the flow of energy through the $r1$ boundary in Figure 8(b). The bulk of the energy flow at this boundary at the beginning of the event is due to the Poynting flux. This circumstance is startling at first, given that the reconnection process should convert the magnetic energy in the current sheet into kinetic and thermal energies. However, the bulk of

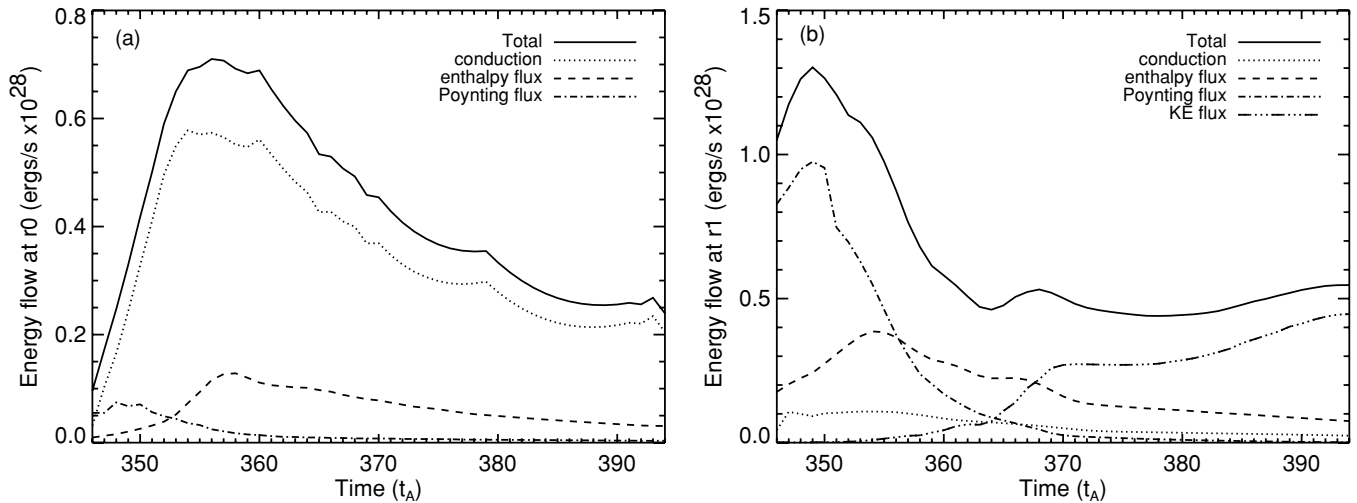


Figure 8. Energy flow over the $r0$ boundary (a) and $r1$ boundary (b) of the control volume. For each plot, we show the total energy through the boundary (solid line), the conduction flux (dotted line), the enthalpy flux (dashed line), and the Poynting flux (dot-dashed line). The kinetic energy flux (dash-dot-dashed line) is shown in the plot of the energy flow over the $r1$ boundary. It is not shown in the plot of the energy flow over the $r0$ boundary, since it is a negligible fraction of the total energy flow. The viscosity term is negligible for both plots.

this Poynting flux term is due to the radial transport of the ϕ component of the magnetic field. This field component is created during the shearing phase, and since it points in the same direction over the current sheet volume, it is not annihilated during reconnection as the eruption progresses.

Toward the end of the eruption, the majority of the energy flux over the $r1$ boundary is due to the kinetic energy flux. This elevated kinetic energy flux is attributable to the reconnection outflow jet. In contrast, the outflow jet at the $r0$ boundary is so small in magnitude that we have not plotted the kinetic energy flux over this boundary in Figure 8(a). The disparity in the magnitude of the upper and lower plasma jets can be explained by the location of the X-point in the current sheet. The X-point forms very low in the current sheet, near the lower boundary, and it remains near the lower boundary throughout the evolution of the event. This circumstance may be a consequence of the fact that the field lines diverge rapidly with height. The height at which the X-line is observed in the simulation tends to be close to the location where the tangential magnetic field outside the current sheet has its maximum value. This location, sometimes referred to as the “pinch point,” is the point where the external magnetic field lines in the immediate upstream inflow regions osculate the sheet (Seaton 2008).

4.3. Flare Emissions and Energy Budget for the Simulated Eruption

Using the temperatures and densities output by our simulations, we can compute the X-ray and extreme ultraviolet (EUV) emissions for the flare loops associated with our modeled CME (see, e.g., Mok et al. 2005; Lionello et al. 2009). The emissions in a given instrument can be found by using the equation

$$I = \int n_e^2(l) f_i(T(l), n_e(l)) dl, \quad (14)$$

where I is the intensity observed in the telescope in units of DN s^{-1} , n_e is the electron density, $f_i(T, n)$ is a function that takes into account the atomic physics and instrument response function, and the integral is done along the line of sight, l . To do these calculations, we have assumed a flare arcade

length of 1×10^5 km. We simulate intensities for the Extreme Ultraviolet Imaging Telescope (EIT) on the *SoHO* and the X-ray telescope (XRT) on the *Hinode* satellite. EIT is a narrow-band imaging telescope that observes wavelengths in the EUV (Delaboudinière et al. 1995). XRT is an X-ray telescope with several broadband filters that image plasma in the 2–15 MK range (Golub et al. 2007). The f_i functions for these telescopes are easily obtainable from the SolarSoft IDL software.

Simulated images in the EIT 195 Å filter and the XRT thin-Be filter, as well as temperature and density, are shown in Figure 9 for four different times after the eruption begins. Reasonable count rates for the two instruments are obtained. Early in the eruption, the prominence-like material is dense and cool, and there is bright emission in the EIT 195 Å line, but the material is not seen at all in the X-rays because it is too cool.

As the event progresses to later times (370 τ_A and 390 τ_A in Figure 9), we see bright, narrow flare loops forming in the EIT 195 Å. This morphology is common in EUV observations of flares (e.g., Warren 2000), and it is due to the narrow temperature sensitivity of the filters on the EIT telescope. The broadband response of the XRT thin-Be filter leads to cusp-shaped loops in the simulated XRT images. This loop morphology is commonly observed in X-ray observations of flares (e.g., Tsuneta et al. 1992; Forbes & Acton 1996; Reeves et al. 2008).

The plasma in the current sheet is between 5 and 10 MK, and it is clearly visible in the X-ray images, even though the density is low in the sheet. The emissions from the current sheet are 2–3 orders of magnitude fainter than the flare loops, but are still bright enough to be detected with a telescope with the dynamic range of XRT. Recently, XRT was able to observe a current sheet-like structure trailing a CME because the associated flare was occulted by the limb of the Sun (Savage et al. 2010).

Another feature evident in the emission images in Figure 9 is a decrease in emission in the areas outside the flare loops and current sheet as the eruption progresses. This decrease is particularly noticeable when comparing the images at 352 τ_A and 370 τ_A . This decrease in emission may correspond to the coronal dimming often seen in X-ray (Sterling & Hudson 1997) and EUV (Zarro et al. 1999; Bewsher et al. 2008) images following a CME. Dimming is thought to be caused by density

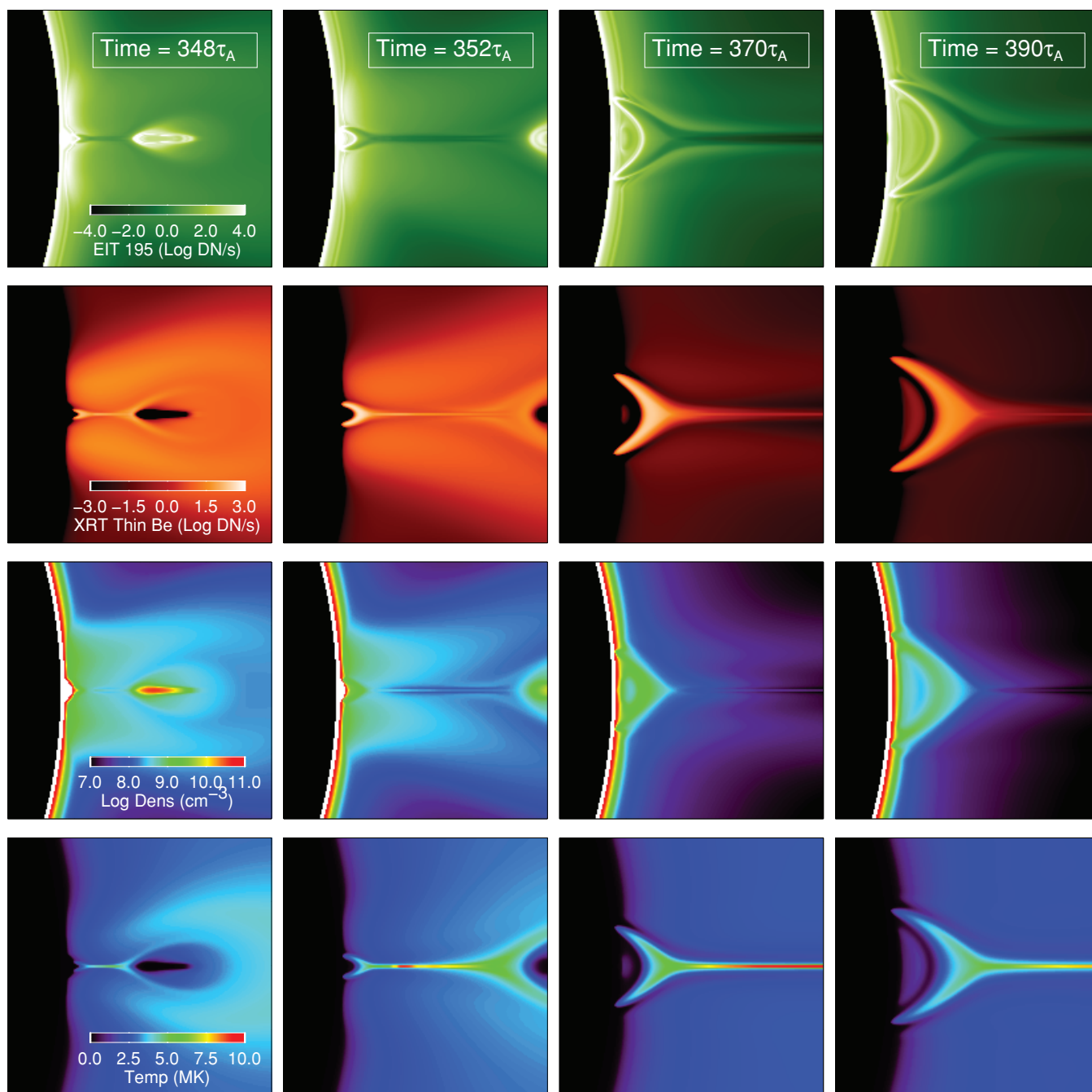


Figure 9. Simulated EIT 195 intensity (top panels), simulated XRT thin Be intensity (second row), log of density (third row), and temperature (bottom panels) for several times after the eruption of the CME. The images have a field of view of $0.5 R_{\odot}$ and the intensity images are log scaled.

depletion as the CME erupts, evacuating the corona beneath it. In the simulation shown in Figure 9, there is a decrease in the density surrounding the flare loops and current sheet between $352 \tau_A$ and $370 \tau_A$, confirming the density depletion hypothesis.

We calculate the energy partition in the simulated eruption in order to compare with observations. We calculate magnetic, kinetic, and gravitational potential energies due to the CME by taking the difference in these quantities pre-eruption ($\tau_A = 347$) and post-eruption ($\tau_A = 393$). The results are shown in Table 1. We divide the energies into similar categories as in Emslie et al. (2005): primary energy (i.e., the magnetic field) and final energies due to the flare (radiative energy) and the CME (kinetic energy and gravitational potential energy). Since our model

is an MHD model, we cannot address energies of accelerated electrons and ions. Emslie et al. (2005) refer to these energies as “intermediate” energies because much of the energy in these non-thermal particles would eventually be converted into energy that heats plasma and causes it to radiate.

To calculate the energy in the CME, we use a control volume that excludes the chromosphere and as much of the solar wind plasma as possible, since these regions are not typically included in calculations of the energy partition that are derived from observations (i.e., Emslie et al. 2004, 2005). This control volume is shown on the top panel of Figure 10, and it has dimensions defined by $r_0 = 1.03 R_{\odot}$, $r_1 = 20 R_{\odot}$, and $\Delta\theta = 0.67$ radians of arc. For these calculations, we assume that the event subtends

Table 1
Comparison of Energies in Simulation and Observations

Energy Type	Simulations ^a	Observations ^b
Primary		
Magnetic	31.5	32.3, 32.3
CME		
Kinetic	30.8 (30.6)	32.3, 32.0
Gravitational Potential	31.7 (31.2)	30.7, 31.1
Flare		
Radiated		
From <i>GOES</i> plasma	29.4	31.3, 31.0
Total from simulation	30.6	

Notes. Energies are in \log_{10} (erg).

^a Simulation values in parentheses are calculated by subtracting a background corona from densities used in calculation.

^b Observation data from the flares of 2002 April 21 (*GOES* class X1.5) and 2002 July 23 (*GOES* class X4.8), respectively. From Emslie et al. (2005).

0.14 radians in the azimuthal direction. This assumption is the same as the assumption of a flare arcade length of 10^5 km that was used above.

We find that the total kinetic energy in the simulated eruption is two orders of magnitude smaller than in the eruptions observed by Emslie et al. (2005). The number for the simulation is reasonable, however, considering that the CMEs studied by Emslie et al. (2005) had speeds of 2300 km s^{-1} and 2600 km s^{-1} at $10 R_s$, and the simulated CME has a speed of only 260 km s^{-1} at $10 R_s$. CMEs with slower velocities observed by Vourlidis et al. (2000) have kinetic energies of the same order as the kinetic energy in our simulation.

The energy due to gravitational potential energy in the simulations is higher than in the eruptions studied by Emslie et al. (2005) and Vourlidis et al. (2000). This difference is because we are able to account for all the mass in the simulation, including particles that are elevated due to the solar wind, while the calculations that are based on observations rely on mass estimates from coronagraph observations and only consider the mass of the CME. A typical method for estimating the mass in a CME using coronagraph observations is to subtract a pre-eruption image that is representative of the background corona from the data containing the CME (Vourlidis et al. 2000; Emslie et al. 2004). If we approximate this background subtraction by subtracting the density from a time near the end of the shearing phase in the simulation ($\tau_A = 270$) from the density used in the calculation of the gravitational potential energy, we get $10^{31.2}$ erg, shown in parenthesis in Table 1. A similar calculation is performed for the kinetic energy, but the background subtraction only reduces this number by a factor of about 1.7.

We also calculate the radiated energy due to flare emissions. For this calculation, we use a small control volume that encompasses only the flare loops. The dimensions of this volume are defined by $r_0 = 1.03 R_s$, $r_1 = 1.18 R_s$, and $\Delta\theta = 0.23$ radians of arc. The boundaries of this control volume are shown on the bottom panel of Figure 10.

We use two methods to determine the radiated energy. First, we directly calculate the radiated energy from the information output by the simulations. We find that the total radiative energy output in the flare loops is 4.2×10^{30} erg, which is 2/3 of the conductive flux found passing through the lower boundary of the current sheet in the last section. Second, we simulate emission from the *GOES* 1–8 Å and 0.5–4 Å bands in order

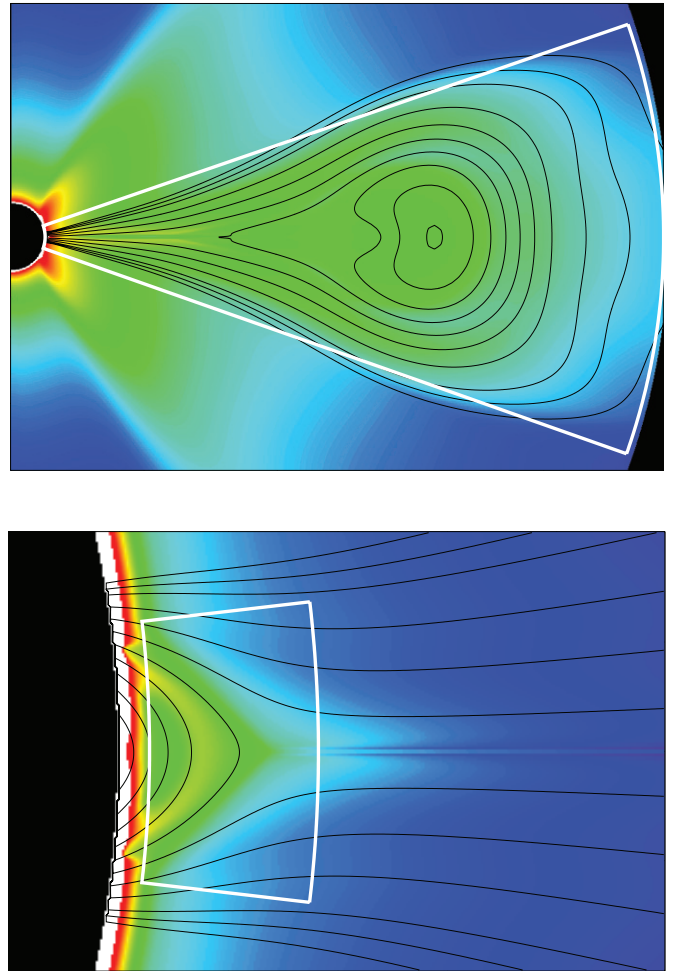


Figure 10. Regions of the simulation domain, shown as white wedges, used to calculate the energy budget for the CME (top) and the radiated energy from the flare (bottom). The images are density and the contours are the magnetic flux at $t = 380 \tau_A$.

to estimate the radiated energy as it would be done from observations. This method uses the assumption that there is negligible conductive cooling, as in Emslie et al. (2005). The numbers for both methods are reported in Table 1. We find that the radiated emissions for the simulated flare are several orders of magnitude lower than the estimates in Emslie et al. (2005), which is to be expected since they examined X flares, and the simulated eruption is a much weaker event. Additionally, we find that the estimate of the radiated energy from *GOES* light curves is an underestimate of the total radiative losses by a factor of about 20. This underestimation is due to radiation in EUV, optical and other wavelengths not accounted for by the *GOES* method.

5. CONCLUSIONS

We have simulated a CME using the 2.5D MHD coronal code MAS, which includes thermal conduction, radiation, and coronal heating. This code allows us to realistically model the thermodynamics in the corona, and thus account for all the sources and sinks of energy that would be present on the Sun. We apply energy diagnostics to this numerical simulation and find that the energy is conserved to within 3% during the stages leading up to the eruption, and to within 4% during the eruption, when the current sheet is formed. These errors are most

likely due to the additional numerical dissipation associated with numerical diffusion.

We use this simulation to examine the energy released in the current sheet during an eruption. Previous examinations of this energy release using semi-analytic loss-of-equilibrium models have been done by Reeves & Forbes (2005) and Reeves et al. (2007). However, these models use the simplifying assumptions that the thermal energy in the flare is derived entirely from the Poynting flux swept into the current sheet, and moreover, that the energy flux out of the current sheet is equally partitioned in the flare loop and CME directions.

Examining our numerical simulation, we find, as expected, that the Poynting flux is the dominant energy flowing into the sides of the current sheet. There is also a large outflow of energy through the sides of the current sheet due to the effects of thermal conduction and viscosity. In our two-dimensional model, a significant portion of the energy transported through the sides of the sheet becomes trapped in the magnetic field lines that encircle the flux rope, and this trapped energy does not contribute to the heating of the flare loops. In three-dimensional models (e.g., Fan & Gibson 2007; Török & Kliem 2005; Lynch et al. 2008), most field lines within the magnetic island map to the solar surface. Therefore, our two-dimensional simulation is likely to underestimate the thermal energy transferred from the reconnection region into the flare ribbons and loops.

We also find that the total energy flow over the current sheet boundary near the flux rope ($r1$) is greater than the total energy flow over the current sheet boundary at the flare loops ($r0$). Early on, before the Poynting flux into the sheet peaks, more than twice as much energy flows out the top boundary as flows out the bottom. However, by the time the Poynting flux peaks, the amounts are roughly the same. During the early phase, the principal component of energy transported through the lower boundary is the heat flux, but the principal component of energy transported through the upper boundary is the Poynting flux associated with the azimuthal magnetic field. The field that reconnects during the initial phase of the eruption is highly sheared, and this shear produces a strong out-of-plane, azimuthal field (i.e., a guide field) in the current sheet. However, by the time of the peak in the Poynting flux, most of this azimuthal field has been expelled from the sheet and the contribution from the Poynting flux is small. During this later phase, kinetic energy is the dominant form of energy transported out the upper boundary, but the dominant form at the lower boundary is still thermal conduction.

The speed of the upward reconnection jet is always much faster than the speed of the downward jet. In some previous planar simulations (e.g., Forbes 1986), the asymmetry in the speeds of the downward and upward jets was found to depend strongly on the plasma beta. For plasma betas on the order of 1, or larger, the downward jet tends to be suppressed, but for plasma betas much less than 1 (typically 0.1 or smaller), downward and upward jets of equal strength can appear if the jet flow becomes supermagnetosonic with respect to the fast-mode wave speed (Forbes & Malherbe 1991). However, the presence of a strong guide field greatly inhibits the formation of a supermagnetosonic jet (Forbes et al. 1989) and this may be one of the main reasons that a strong downward jet never formed in our simulation.

We simulate the X-ray and EUV flare emissions associated with this eruption. We find that the simulated emissions produce flare loop morphologies that are similar to observed structures, including narrow, bright EUV loops, and cusp-shaped X-ray loops. The simulation produces a dimming effect seen in the

regions around the simulated flare that is similar to coronal dimmings seen in the aftermath of observed eruptions. In our simulation, this dimming effect is due to an evacuation of plasma as the CME erupts. We also find that structures associated with the current sheet should be visible in the soft X-rays, given sufficient sensitivity.

We examine the global energy partitioning in the simulated eruption. The values for the various types of energy calculated in this way are reasonable given that the simulated eruption is weaker than most observed events where this kind of calculation has been done. We find that calculations of the radiative losses using only X-ray observations (i.e., the GOES 1–8 Å channel) underestimate the real radiative losses by a factor of about 20.

In this study, we have taken advantage of the simplicity and symmetry afforded by a 2.5D simulation. In the future, we plan to do a similar analysis on more realistic three-dimensional models of coronal eruptions, which are considerably more complex.

K.K. Reeves thanks E. E. DeLuca and H. D. Winter for useful conversations about the numerical simulations. K.R. and T.F. are supported under the NSF-SHINE program, grant number ATM0752257. Additional support for K.R. is provided by NASA grant NNM07AA02C to the Smithsonian Astrophysical Observatory. The work of J.L. and Z.M. is supported by NASA's Heliophysics Theory, LWS, and SR&T Programs, the LWS Strategic Capabilities Program (NASA, NSF, and AFOSR), and the Center for Integrated Space Weather Modeling (an NSF Science and Technology Center).

REFERENCES

- Athay, R. G. 1986, *ApJ*, 308, 975
 Bewsher, D., Harrison, R. A., & Brown, D. S. 2008, *A&A*, 478, 897
 Birn, J., Borovsky, J. E., & Hesse, M. 2008, *Phys. Plasmas*, 15, 032101
 Birn, J., Fletcher, L., Hesse, M., & Neukirch, T. 2009, *ApJ*, 695, 1151
 Chen, Y., Hu, Y. Q., & Sun, S. J. 2007, *ApJ*, 665, 1421
 Craig, I. J. D., & Litvinenko, Y. E. 2009, *A&A*, 501, 755
 Delaboudinière, J.-P., et al. 1995, *Sol. Phys.*, 162, 291
 Emslie, A. G., Dennis, B. R., Holman, G. D., & Hudson, H. S. 2005, *J. Geophys. Res. (Space Phys.)*, 110, 11103
 Emslie, A. G., et al. 2004, *J. Geophys. Res. (Space Phys.)*, 109, 10104
 Fan, Y., & Gibson, S. E. 2007, *ApJ*, 668, 1232
 Forbes, T. G. 1986, *ApJ*, 305, 553
 Forbes, T. G. 2000, *J. Geophys. Res.*, 105, 23153
 Forbes, T. G., & Acton, L. W. 1996, *ApJ*, 459, 330
 Forbes, T. G., & Malherbe, J. M. 1991, *Sol. Phys.*, 135, 361
 Forbes, T. G., Malherbe, J. M., & Priest, E. R. 1989, *Sol. Phys.*, 120, 285
 Golub, L., et al. 2007, *Sol. Phys.*, 243, 63
 Hollweg, J. V. 1978, *Rev. Geophys. Space Phys.*, 16, 689
 Hollweg, J. V. 1986, *ApJ*, 306, 730
 Ko, Y.-K., Raymond, J. C., Lin, J., Lawrence, G., Li, J., & Fludra, A. 2003, *ApJ*, 594, 1068
 Lin, J., Ko, Y.-K., Sui, L., Raymond, J. C., Stenborg, G. A., Jiang, Y., Zhao, S., & Mancuso, S. 2005, *ApJ*, 622, 1251
 Lin, J., Li, J., Forbes, T. G., Ko, Y.-K., Raymond, J. C., & Vourlidas, A. 2007, *ApJ*, 658, L123
 Linker, J. A., Lionello, R., Mikić, Z., & Amari, T. 2001, *J. Geophys. Res.*, 106, 25165
 Linker, J. A., & Mikić, Z. 1995, *ApJ*, 438, L45
 Linker, J. A., & Mikić, Z. 1997, in *Coronal Mass Ejections*, ed. N. Crooker, J. Joselyn, & J. Feynman (Geophys. Monograph, Vol. 99; Washington, DC: AGU), 269
 Linker, J. A., Mikić, Z., Lionello, R., Riley, P., Amari, T., & Odstrčil, D. 2003, *Phys. Plasmas*, 10, 1971
 Linker, J. A., et al. 1999, *J. Geophys. Res.*, 104, 9809
 Lionello, R., Linker, J. A., & Mikić, Z. 2001, *ApJ*, 546, 542
 Lionello, R., Linker, J. A., & Mikić, Z. 2009, *ApJ*, 690, 902

- Lionello, R., Mikić, Z., & Linker, J. A. 1999, *J. Comput. Phys.*, **152**, 346
- Lynch, B. J., Antiochos, S. K., DeVore, C. R., Luhmann, J. G., & Zurbuchen, T. H. 2008, *ApJ*, **683**, 1192
- MacNeice, P., Antiochos, S. K., Phillips, A., Spicer, D. S., DeVore, C. R., & Olson, K. 2004, *ApJ*, **614**, 1028
- Manchester, W. B., Gombosi, T. I., Roussev, I., De Zeeuw, D. L., Sokolov, I. V., Powell, K. G., Tóth, G., & Opher, M. 2004, *J. Geophys. Res. (Space Phys.)*, **109**, 1102
- Mikić, Z., & Linker, J. A. 1994, *ApJ*, **430**, 898
- Mikić, Z., Linker, J. A., Schnack, D. D., Lionello, R., & Tarditi, A. 1999, *Phys. Plasmas*, **6**, 2217
- Mok, Y., Mikić, Z., Lionello, R., & Linker, J. A. A. 2005, *ApJ*, **621**, 1098
- Moore, R., et al. 1980, in *Solar Flares: A Monograph from Skylab Solar Workshop II*, ed. P. A. Sturrock (Boulder, CO: Univ. Colorado Press), 341
- Reeves, K. K., & Forbes, T. G. 2005, *ApJ*, **630**, 1133
- Reeves, K. K., Seaton, D. B., & Forbes, T. G. 2008, *ApJ*, **675**, 868
- Reeves, K. K., Warren, H. P., & Forbes, T. G. 2007, *ApJ*, **668**, 1210
- Savage, S. L., McKenzie, D. E., Reeves, K. K., Forbes, T. G., & Longcope, D. W. 2010, *ApJ*, in press
- Seaton, D. B. 2008, PhD thesis, Univ. New Hampshire
- Seaton, D. B., & Forbes, T. G. 2009, *ApJ*, **701**, 348
- Sterling, A. C., & Hudson, H. S. 1997, *ApJ*, **491**, L55
- Sui, L., & Holman, G. D. 2003, *ApJ*, **596**, L251
- Török, T., & Kliem, B. 2005, *ApJ*, **630**, L97
- Tsuneta, S., Hara, H., Shimizu, T., Acton, L. W., Strong, K. T., Hudson, H. S., & Ogawara, Y. 1992, *PASJ*, **44**, L63
- Vourlidas, A., Subramanian, P., Dere, K. P., & Howard, R. A. 2000, *ApJ*, **534**, 456
- Warren, H. P. 2000, *ApJ*, **536**, L105
- Yokoyama, T., & Shibata, K. 1997, *ApJ*, **474**, L61
- Zarro, D. M., Sterling, A. C., Thompson, B. J., Hudson, H. S., & Nitta, N. 1999, *ApJ*, **520**, L139